Multiple remote sensing assessment of the catastrophic collapse in Langtang Valley induced by the 2015 Gorkha Earthquake

Hiroto Nagai[1], Manabu Watanabe[2], Naoya Tomii[3], Takeo Tadono[1], Shinichi Suzuki[1]

[1]Earth Observation Research Center, Japan Aerospace Exploration Agency, 2-1-1 Sengen, Tsukuba, Ibaraki, 305-8505, Japan
[2]School of Science and Engineering, Tokyo Denki University, Ishizaka, Hatoyama-machi, Hiki-gun, Saitama, 305-0394, Japan
[3]Satellite Applications and Operations Center, Japan Aerospace Exploration Agency, 2-1-1 Sengen, Tsukuba, Ibaraki, 305-8505, Japan

Correspondence to: Hiroto Nagai (nagai.hiroto@jaxa.jp)

Abstract. We demonstrated an assessment of the sediments caused by a catastrophic avalanche, induced by the main shock of the 2015 Gorkha Earthquake in Nepal. Calculation of decreasing coherence and visual interpretation of amplitude images by means of the Phased Array-type L-band Synthetic Aperture Radar-2 (PALSAR-2) have a high potential for delineating the hazardous zone. These delineated outlines area highly consistent with that from a high-resolution optical image of WorldView-3 (WV-3). The delineated sediment collapse areas were estimated as 0.63 km^2 (PALSAR-2 coherence calculation), 0.73 km^2 (PALSAR-2 visual interpretation), and 1.09 km^2 (WV-3), respectively. In the WV-3 image, surface features were classified into 15 segments, with the flowing, scattering, and other characteristics implying different physical properties. Our findings suggest that the avalanche event did not supply a homogeneous snow-and-ice material with debris but supplied multiple kinds of sediments from sequential collapse in a short period. By means of satellite-derived pre- and post-event digital surface models, differences in the surface altitudes of the collapse events estimated the total volume of the sediments as 6229.1 $\times 10^3$ m^3, with an error possibility between 5363.3$\times 10^3$ to 7314.8$\times 10^3$ m^3, most of which are distributed along the river bed and the water stream. Further altitude measurements after ice/snow melting would reveal a contained volume of melting ice and snow, which will contribute to numerical avalanche simulation and source considerations.

Keywords. ALOS-2, InSAR, WorldView-3, ALOS World 3D, avalanche, Nepal, Himalaya

1 Introduction

A great earthquake of 7.8 Mw, namely the 2015 Gorkha Earthquake, occurred in the district of Lamjung, central Nepal on April 25, 2015 (Ge et al. 2015; Parameswara et al. 2015), which caused more than 9,000 deaths and 23,000 people to be injured (e.g., Roy et al. 2015). Damages in urban areas were especially caused on stone/brick masonry structures (Goda et al. 2015), whereas numerous landslides were induced in rural/mountain areas (ICIMOD 2015a; Kargel et al. 2015).

The most catastrophic collapse in the mountainside was reported in the Langtang valley, located 70 km north of Kathmandu (ICIMOD 2015b; Kargel et al. 2015). Landslides, avalanches, and sudden air pressure wave traveled from a south-facing steep slope to the bottom of a U-shaped valley. The fallen materials, i.e., a mass of boulders, snow, and ice, covered the valley bottom involving almost all of the buildings in Langtang Village. At the opposite side of the valley, trees were prostrated and lost their leaves by the sudden air pressure wave. More than 170 villagers (reaching its double including trekkers and porters) were killed (or left missed) in this event.

Damage detection through SAR technique has been applied for urban damaged areas (e.g., Kobayashi et al, 2011; Yonezawa and Takeuchi, 2001; Tamura and El-Gharbawi, 2015; Watanabe et al., 2016), but almost no case for a large-scale mountain hazard was studied. We apply SAR damage detection for the avalanche case. In addition, a detailed interpretation of the damaged area by means of high-resolution optical satellite imagery coupled with sediment volume estimation would provide detailed features of this avalanche. In this study, we demonstrate (1) the identification with synthetic aperture radar (SAR) for urgent response, (2) the mapping and interpretation of physical property with high-resolution optical imagery, and (3) the volume estimation using the difference between pre- and post-event digital surface models (DSMs). These results are then compared to evaluate effectiveness of SAR analysis for hazard response and to discuss initial situation of this collapse.

2 Data set and Processing

2.1 Study site

The catastrophic collapse was caused in the middle of Langtang Valley (28º12'50"N, 85º30'5"E), one of the national parks in Nepal (Fig. 1). The main river in this valley, the Langtang Khola, flows from the east to the west, and joins the main stream, Bote Kosi (Trisuli Gandaki), at the end of the valley near a village, Syabru Bensi (Ono and Sadakane 1986). The length of the valley is approximately 50 km, and the width ranges from 1 to 2 km. A typical U-shaped valley formed by glaciation. The Lirung, Khyimjung, Yala, Shalbachum, Langtang, and Langshisa glaciers are located 4100 m above sea level (a.s.l.). In addition, several unnamed glaciers are distributed along both the ridges of the U-shaped valley (Shiraiwa and Watanabe 1991), where Mt. Langtang Lirung is the highest peak (7239 m a.s.l.).

The Lantang valley consists of the Gosainkund gneiss zone (various gneisses and granitic migmatite) and the Langtang Himal migmatite zone (medium-grained garnet-mica-gneiss of granitic composition and coarse-grained augen-gneiss) (Arita et al. 1973; Shiraiwa and Watanabe 1991). Six successive glacial stages were recognized from an in-situ dating survey on moraine compositions (Shiraiwa and Watanabe 1991; Shiraiwa, 1994). Relatively extensive glaciation in the Langtang Stage (3650–3000 yr BP) is suggested in the late Quaternary. Permafrost is not highly expected in this valley because of the large amount of winter snow, which prevents deep freezing in winter (Shiraiwa, 1994).

The Langtang Valley is a famous trekking course for tourists, and it has been called "one of the most beautiful valleys in the world." The village of Langtang was called "Yul" by the villagers (Ono and Sadakane 1986). The main local occupations are

farming and tourism. Many temporary houses called "Kalkha" were built around the village for livestock farming, i.e., for the transhumance of yaks.

2.2 Synthetic aperture radar imagery

In order to estimate the damages after the earthquake on April 25, the Japan Aerospace Exploration Agency carried out an emergency observation with the Phased Array type L-band Synthetic Aperture Radar-2 (PALSAR-2) onboard the Advanced Land Observing Satellite-2 (ALOS-2, "DAICHI-2") aiming central Nepal at 7:02 on April 26 (GMT). This image was taken on the left-looking strip-map mode with a 3-m spatial resolution along the descending orbit of Path 55. Visual interpretation of the orthorectified backscatter amplitude image of HH polarization (product level 2.1) was performed. A pre-event PALSAR-2 image taken at 6:13 on December 28, 2014 was used for comparison. This image was taken in a right-looking strip-map mode with a 3-m spatial resolution along the descending orbit of Path 48. Visual interpretation of the orthorectified backscatter amplitude image of HH polarization (product level 2.1) was simultaneously performed.

Not only the amplitude imagery but also the phase information emitted and received by the synthetic aperture radar (SAR) contributes to the situational awareness. We performed coherence calculation using interferometric phase information of SAR, which was explained by Plank (2014) in detail. Coherence can be calculated from two SAR images observing an identical place twice from the same orbit and incidence angle, thereby achieving similar phase and intensity information of the receiving microwave, which is calculated for a pair of SAR images by

$$\gamma = \frac{E\langle c_1 c_2^* \rangle}{\sqrt{E\langle c_1 c_1^* \rangle E\langle c_2 c_2^* \rangle}} \qquad (1)$$

where c_1 and c_2 are the corresponding complex-valued pixels of the two images, c^* is the complex conjugate of c, and E indicates the expected value. The detailed mathematical procedure is described in Touzi et al. (1999) and López-Martínez and Pottier (2007). A significant change in surface feature between two observations results in lower coherence (in other words, lower similarity). Other noisy influences, including vegetation growth, can be reduced by calculating normalized differences with a coherence calculated from two pre-hazard images. The normalized coherence decrease (NCD) is calculated as

$$\gamma_{diff} = \frac{\gamma_{pre} - \gamma_{int}}{\gamma_{pre} + \gamma_{int}} \qquad (2)$$

where γ_{pre} is the coherence value between two images before the earthquake (October 4, 2014 and February 21, 2015), and

γ_{int} is the coherence value between the two images over the earthquake (February 21 and May 2, 2015). These data were acquired from a same orbit with a spatial resolution of 10 m. When γ_{int} is calculated for images over a hazard, higher-valued pixels of γ_{diff} indicate the reduction of the similarity, which has high potential of hazard-induced deformation or destruction. Several previous studies applied this method using L-band SAR for damage detection in urban areas (e.g., Kobayashi et al., 2011; Yonezawa and Takeuchi, 2001; Tamura and El-Gharbawi, 2015; Watanabe et al., 2016), but no such study applied this

3

method for mountain hazard. Throughout this study, we aim to emphasize the possibility of normalized conference difference by using L-band SAR for damage detection in mountain regions.

Numerous noises are removed by focal statistics. In the NCD raw image, all pixel values are overwritten by the mean values within 15-pixel circles around each pixel (Fig. 2). This filter emphasizes the concentration of high values, whereas the homogeneously scattered high values are de-emphasized. The detailed steps are as follows:

1. The radius of a window circle is set as 15 pixels.
2. A mean value of the pixels in a circle is calculated.
3. The mean value is placed in the center pixel of the circle.
4. Moving the circle, every pixel on the output image is filled with the mean values in the same way.

2.3 Pre-event optical imagery and DSM

Pre-event optical satellite imagery and its three-dimensional view were generated to grasp the previous situation in further details. Images of the Panchromatic Remote-sensing Instrument for Stereo Mapping (PRISM) and the Advanced Visible and Near Infrared Radiometer type 2 (AVNIR-2) onboard the Advanced Land Observing Satellite (ALOS) were acquired at 5:02 on October 12, 2008, which were combined into a orthorectified pan-sharpened image. It is a visible color image with a spatial resolution of 2.5 m. A DSM dataset "ALOS World 3D (AW3D)" was used for this study. AW3D was generated from numerous (>3 million scenes) PRISM nadir, forward, and backward images, which were taken through ALOS operation period (2006 to 2011), automatically stacked, and synthesized into a global DSM dataset with a horizontal spacing of 5 m (Tadono et al., 2015). In addition to its finer resolution than existing datasets such of the Suttle Radar Topography Mission (SRTM) and the Global Digital Elevation Model by Advanced Spaceborne Thermal Emission and Reflection Radiometer (ASTER GDEM) (larger than 30 m), occasional anomaly values was excluded in the generation process as well as occasional cloud cover filled with other scenes. As a result, an accuracy of 4.10 m root mean square for the vertical component versus globally distributed ground control points (4622 points) was reported (Tadono et al., 2015). The orthorectified pan-sharpened image was overlain on the AW3D DSM with a pixel spacing of 5 m to show a three-dimensional view for interpretation.

2.4 Post-event optical imagery and DSM

Post-event optical satellite imagery and DSM were used to recognize the damaged situation in detail. A DigitalGlobe's satellite, WorldView-3 (WV-3) observed the Langtang valley on May 8, 2015, with a panchromatic sensor of 0.31 m spatial resolution and a multispectral sensor of 1.24 m spatial resolution to generate a set of pan-sharpened stereo pair imagery. Using these data, a post-event DSM in a pixel spacing of 2 m was produced by NTT DATA as its commercial service. The DSM is generated by stereo photogrammetric method using two WV-3 images acquired on May 8, 2015 using stereo-area-collect mode (26.2 km swath, 112 km path). Two images that are (1) forward looking with cross-track tilting to the west hand (i.e., average off-nadir angle: 27º, average target azimuth: 245º /scene id: 104001000BA62E00) and (2) backward

looking with cross-track tilting to the west hand (i.e., average off-nadir angle: 27º, average target azimuth: 319º /scene id: 104001000B3B2300) were acquired. Spatial resolution after cross-track tilt was 0.38 m, coarsened from 0.31 m because of tilting. DSM generation flow (i.e., stereo matching, RPC ortho-rectification, pixel resampling, and DSM data output) was performed by NTT DATA with their original software, where the geo-referencing process was supported by WV-3 accurate orbit information without any in-situ ground control point and a resampled pixel spacing of 2 m. Officially announced specification shows a vertical accuracy of 4 m and a horizontal accuracy of 5 m as root mean square errors. In two sites that are neighboring the sediment surface, relative calibration/validation of this DSM and the AW3D DSM was performed and summarized in a supplementary material, in which a standard deviation error of 1.5 m between WV-3 and AW3D DSM is reported. A pan-sharpened image (high-resolution and composite-color image) generated from one scene of the pair was orthorectified by an author with 178 tie points onto the PRISM image taken on October 12, 2008.

3 Results

3.1 SAR amplitude imagery

A post-event PALSAR-2 backscatter amplitude image is shown in Fig. 3a, and a pre-event image is shown in Fig. 3b. The brightness of these images corresponds to the amplitude of microwave signal reflected to the PALSAR-2 antenna. The difference between the two represents a completely modified surface feature. The mass of the sediment is identifiable only in the post-event image within an area of 0.73 km^2 (centroid: 28º12'54"N, 85º30'14"E), ranging approximately 1500 m from the upstream to the downstream of the Langtang Khola and 700 m from the upper to the bottom part of the U-shaped valley. Comparing the pre-event PALSAR-2 backscatter amplitude image (Fig. 3b) and an ALOS PRISM/AVNIR-2 pan-sharpened image taken on October 12, 2008 (Fig. 3c), bright points and a valley-shaped feature correspond to buildings and water streams, respectively. These features completely disappear in Fig. 3a, which means that they have been filled by the sediment mass after the quake. A three-dimensional view of the ALOS PRISM/AVNIR-2 image overlaid on the AW3D DSM is shown in Fig. 3d. This sediment area is located below the terminus of a glacier on the north-facing slope. Another glacier flows toward the debris-covered area of the former glacier. This geography suggests a possibility that a large volume of materials travelled from these glaciers with an extremely high potential energy.

3.2 SAR coherence decrease

NCD is calculated from the PALSAR-2 images (Fig. 4a). NCD values greater than 0.2 are reclassified into multiple colors with 0.05 steps, in which scattered NDC dots are difficult to be identified (Fig. 4a). After a focal statistics process with the 15-pixel circle, noisy pixels were moderated and several parts with a high NCD appeared (Fig. 4b). One of the high-value areas (>0.2) correspond to the sediment outline delineated from the PALSAR-2 amplitude image (p in Fig. 4b). Separated from a connecting upper outline at the narrowest part (< 5-pixel width), this part has an area of 0.63 km^2 with a centroid of [28º12'57"N; 85º30'14"E]. Visual interpretation of the amplitude images (Fig. 3) and NCD calculation (Fig. 4) yield a

5

similar result for the collapsed sediments (Fig. 4). Moreover, the both methods are not hindered by the cloudy weather, and hence, have a great potential to immediately indicate a catastrophic collapse and contribute to decision-making for such hazards in the monsoon season.

Furthermore, above the sediment mass, two parts on the south-facing slope show high-NCD concentrations in (q) 0.22 km^2 and (r) 0.07 km^2 areas (Fig. 4b). They are located at the downstream periphery of the Glacier Termini, suggesting the consequent collapse from the tributary glacier to the main glacier. High NCD does not appear on the glacier surfaces possibly because frequent avalanches and glacier flows cause regular changes in the surface. For such surfaces, the changes uniquely caused by an earthquake could be identified by NCD calculation.

3.3 Collapse mapping with a post-event optical imagery

Identification and mapping of the surface features were performed by interpreting the high-resolution satellite imagery (Fig. 5a). In total, 1.09 km2 sediment cover is delineated including apertures (no-sediment patches), whereas three inclusive parts have little sediment exposure (Ap. 1 to 3). The surface features were classified into 15 segments (Seg. 1 to 15) by interpreting the sediment darkness, flow, scatter, and other surface characteristics (Fig. 5a; Table 1).

According to the sediment darkness interpreted with the WV-3 image, segments were classified into "dark" (Seg. 1 to 4), "light" (Seg. 5 and 6), "medium" (Seg. 7 to 11), and "dark" (Seg. 12 to 15) groups (Table 1). Further, Segs. 1 and 2 have relatively large area of apertures between sediment-covered surfaces, which implies that the materials have scattered directly from the mountainside without flowing. Similar darkness is seen in Segs. 3 and 4, with the former having some areas of apertures (scattering) and the latter consistently flowing downstream in a narrow path connecting to Seg. 5 without aperture. Segment 5 has a consistent flow to the downstream, filling the path of the water stream (see Fig. 3c) with identifiable boulders, whereas Seg. 6 has bright streaks along its flow rather than boulders. Segments 7 to 11 have similar medium darkness, in which Seg. 7 has a flowing feature and Seg. 9 has an additional mud-like feature filling the riverbed in the upstream of Seg. 5. Segments 10 and 11 are located at the opposite side of the U-shaped valley beyond the river (i.e., on a north-facing slope), with Seg. 11 having a much scattered (splashed) distribution. Moreover, prostrated trees are identifiable in Seg. 11. Segments 12 to 15 have darker sediments as compared to Segs. 7-11. Additionally, Segs. 13 and 15 have large apertures, and Seg. 14 is detached from the main sediment mass.

Classifying the sediment surfaces into several segments suggests that this collapse contains various kinds of sediment sources. Multiple layers of sediments with different origin, volume, viscosity, and other surface features do not suggest a single (instant) collapse episode, but imply a continuous sequence of falling from multiple sources in a short period of time.

3.4 Surface elevation changes

According to the relative calibration/validation of the AW3D and WV-3 DSMs (see the Supplementary material), An horizontal offset of 5 m (1 pixel) to the west and an altitude offset of +27.0 m were added to the AW3D DSM to meet the WV-3 DSM with the best consistency. Possible altitude error of 1.5 m was given to calculate minimum and maximum

6

volumes. After the calibration and validation, the difference between the post-event WV-3 DSM and the pre-event AW3D DSM revealed an increase in surface altitude in the collapse site reaching a maximum of 46.7 m (Fig. 5b; Table 1). The increase in the altitude was especially pronounced in Segs. 5 and 9 along the river bed (Fig. 5), which was likely caused by sediment deposition. In these segments, the mean increase in altitude are 20.3 m and 22.0 m, respectively; whereas mean values smaller than 3 m or those no greater than 11 m were measured on other segments. Considering the potential DSM accuracy (see the Supplementary material), changes in a scale of 1.5 m have a greater dominance of uncertainty. We note that the negative values are replaced by 0 to avoid any unnatural errors.

Calculating the altitude change and surface area, a total volume of 6229.1×10^3 m^3 was estimated without error consideration. Most of the volume belongs to Seg. 5 (3612.6×10^3 m^3; 58.0%) followed by Seg. 9 (1036.5×10^3 m^3; 16.7%). In order to figure out the possible range of volume estimation uncertainty, we assumed 1.5 m as the error range for altitude measurements. When the altitude change in every segment is homogeneously underestimated to be 1.5 m and the negative values are replaced by 0, the total volume is then estimated to be 5363.3×10^3 m^3 (Table 1). When the altitude change in all areas is homogeneously overestimated to be 1.5 m, the total volume is estimated to be 7314.8×10^3 m^3. In these estimations, +1.5 m offset is also given to the aperture patches because they were difficult to be excluded manually. The real sediment volume is thus estimated to be around 6229.1×10^3 m^3, no smaller or greater than that range.

4 Discussion

4.1 SAR-derived surface changes

The sediment outline delineated from the PALSAR-2 amplitude image has an area of 0.73 km^2, which is very close (i.e. contained area difference smaller than 5%) to what Kargel et al. (2015) measured with DigitalGlobe's high-resolution optical satellite images (0.751 to 0.761 km^2). Hazard scale is thus able to be known similarly by the both methods. The outline delineated from the PALSAR-2 image reaches 67.0% of the area obtained from the WV-3 image with detail visual interpretation including scattered materials (1.09 km^2) (Fig. 6). Its spatial coverage corresponds to Segs. 5, 6, 7, 8, 9, 12, 13, and parts of Segs. 4 and 14. Most of the flowing segments are included in that coverage, whereas most of the scattered segments are excluded (Fig. 6; Table 1). It suggests that scattered materials are difficult to be recognized with a 3-m spatial resolution of PALSAR-2 imagery. Furthermore, sediments on the north-facing slopes are also ignored. Possibly, the microwave reflection from/to PALSAR-2 was hindered by the very steep mountain hillslope.

The sediment outline extracted by NCD calculation has an area of 0.63 km^2, which is 58.0% of that from the WV-3 image. Its spatial coverage corresponds to Segs. 6, 7, 8, 12, 13, 14, and parts of Ap. 1, Seg. 3, and Seg. 5, whereas Segs. 9, 10, 11, and 15 are missed. NCD indication on the little coverage of sediments on Ap. 1 can be explained if the surface materials before the avalanche were extensively blown away (e.g., from vegetation to bare terrain). No NCD indication along the riverbed is explainable by the geomorphic alternation constitutively caused by the river erosion, which de-emphasizes the avalanche-caused change in the NCD index. North-facing slopes were covered by forestry, where little NCD is explainable

7

owing to growing trees and seasonal defoliation. Two extra parts of high NCD value caused on the valley bottom (i.e. villages of Chyamki and Singdum) ((s) in Fig. 4b) are corresponding to other collapse occurrences which were identifiable with an optical image shown in Fig. S6c of Kargel et al. (2015).

The geospatial information derived from PALSAR-2 is, thus, usable for disaster response, although the microwave characteristics should be carefully considered. Without pre-event archived data from the same orbit, interferometric SAR technique cannot be used. Instead, a post-event backscatter amplitude image is to be interpreted visually with assistance of other satellite images. The visual interpretation needs careful examination by changing the brightness and contrast of the image, because microwave reflection is influenced simultaneously by both the physical properties and the geomorphic shape of the target area. Through this observation, we have recognized that the visual identification of an unknown hazard only using images is difficult. Therefore, we needed some information about the place and the type of hazard being investigated before interpretation so far. Nevertheless, the approximate scale of the collapse was successfully recognized and provided to the related authorities for emergency response.

Accumulation of the archived data more than once from each orbit enables the coherence normalization to emphasize the unusual coherence decrease by a hazard. Furthermore, removing the small patches by means of focal statistics successfully resulted in sediment extraction, which is highly consistent with that from an optical satellite image. For other kind and scale of hazards, the parameter settings (i.e., circle size to obtain a mean value) needs to be assessed and validated through several case studies. We have confirmed that the NCD calculation cannot be used for slightly, but constitutively changing terrains, such as river beach and vegetation.

In terms of the avalanche source, we found two parts of high NCD values above the collapse sediment on the hillslope ((q) and (r) in Fig. 4b). On the glacier surfaces, regular flowing could de-emphasize the unusual change caused by the avalanche or other collapse events, even if they had happened. The two parts suggest that the falling materials went through these parts and altered their surface features. We could not detect the drastic surface changes in the uphill between AW3D (pre-event) and WV-3 (post-event) images, but Lacroix (2016) supported our suggestion by comparison of DSMs generated from Satellite Pour l'Observation de la Terre (SPOT). Such an extremely-steep slope is difficult to obtain an accurate DSM from most of satellite images, therefore NCD would be preferable focus to be coupled with DSM comparison.

4.2 Details of the avalanche event

At an early time, Kargel et al. (2015) defined this event as a landslide, but they also mentioned "co-seismic snow and ice avalanches and rockfalls" with an image of lower surface temperature observed by Landsat-8 thermal infrared sensor. Lacroix (2016) defined it as a debris avalanche composed mostly of ice and discussed its triggers around the mountain ridge above two glaciers. Fujita et al. (2016) confirmed sediment boulders on the surface, including melting ice (Fig. 7) and rapid surface lowering after the quake, through an in-situ survey, thereby suggesting that contained ice and snow were melting under the debris. Fujita et al. (2016) concluded that extremely heavy snowfall before the quake increased its volume, a

finding that was coupled with weather station data. Therefore, we think this event should be defined as "a catastrophic avalanche event including debris and glacier ice" in our introduction.

Our finding from the interpretation of a high-resolution WV-3 image suggests several layers of the sediment. Multiple segments of the collapsed sediment classified with a WV-3 image imply different sediment sources that have fallen continuously in a short period of time, generating sediment layers (Fig. 5). We could not interpret their layer sequence in detail, but found the different physical properties, i.e., directly fallen and scattered within those places and/or once fallen and flowing the downstream. Especially, Segs. 10 and 11 are located at the end of the flowing parts (Seg. 7 to 9) and splashed onto the opposite hillslope, which implies extremely high potential energy from the source to leap for this range (> 500 m). Splashing direction of Seg. 11 is consistent with the direction of the prostrated trees, which implies that the extreme air pressure happened at the same time of this splashing.

Thick layers of sediments are interpreted in Segs. 5 and 9 as well as the river-side parts of Segs. 4 and 10. A large volume of the muddy sediments in Seg. 9 is likely to have traveled through Seg. 7, by which the local buildings (Fig.3c) were destroyed and swept away. On the other hand, the pre- and post-avalanche DSM difference estimated the thinner sediment layers (within an uncertain small scale for the DSM accuracy) in Segs. 6, 7, and 12, regardless of their complete coverage without the aperture. Thin layers (< 5 m) remain after the avalanche with little dominance of volume.

Kargel et al. (2015) estimated total mass of this sediment as ~3.3×10^9 kg, assuming homogeneous thickness of 2 m on its entire surface. Our study revealed heterogeneous volume distribution, which is especially concentrated along the water streams. According to the assumed density of 2200 kg m^{-3} (Kargel et al., 2015), our estimated volume (6229.1×10^3 m^3) turns out to be 11.5×10^9 kg, reaching 3.5 times of the former (Kargels') estimation. Our volume estimation is rather similar to the estimation obtained by Lacroix (2016) through a comparison of SPOT-derived DSMs (6950×10^3 m^3) with a small difference (~10%). Furthermore, Fujita et al. (2016) performed an in-situ survey from which they estimated the total volume of the avalanche sediment as 6.81×10^6 m^3, which is 109% of what we estimated. Thus, a comparison with the satellite-based studies by Kargel et al. (2015) and Lacroix (2016) indicates that our estimated sediment volume is within the most equivalent order to that from the in-situ measurement by Fujita et al. (2016).

5 Conclusion

Initial multi-satellite observation and assessment were carried out for the catastrophic avalanche induced by the 2015 Gorkha Earthquake in Nepal on April 25. Radar observation by means of PALSAR-2 resulted in two successful ways of backscatter amplitude image and coherence analysis, which are both usable for urgent hazard response to acquire quantitative information, not hindered by frequent cloud cover in those regions during monsoon. Detailed visual interpretation and classification of the sediments with a WV-3 pan-sharpened image revealed the multiple physical properties, which suggest the sequential failure of materials from different sources. The difference between the pre- and post-event DSMs estimated a total sediment volume of 6229.1×10^3 m^3 (11.5×10^9 kg as weight), of which the dominant mass is accumulated along the

water streams. Other material-covered surfaces do not have measurable thickness of sediment. The muddy features interpreted in some of them imply high ice and snow content. Coupling further altitude measurements with temporal intervals would clarify the surface lowering by ice/snow melting, for which the water content estimation is invaluable as one of the input data for avalanche simulation and source consideration.

Author contribution

H. Nagai designed the total analysis and discussion. M. Watanabe carried out InSAR coherence calculation and improved the manuscript. N. Tomii organized use of WorldView-3 image. T. Tadono and S. Suzuki managed ALOS-2 observation.

Competing interests

The authors declare that they have no conflict of interest.

References

Arita, K., Ohta, Y., Akiba, C., and Maruo, Y.: Kathmandu region. In. Hashimoto, S. (ed.), Geology on Nepal Himalayas, Sapporo, Saikon Publishing, 99–145, 1973.

Fujita, K., Inoue, H., Izumi, T., Yamaguchi, S., Sadakane, A., Sunako, S., Nishimura, K., Immerzeel, W. W., Shea, J. M., Kayashta, R. B., Sawagaki, T., Breashears, D. F., Yagi, H., and Sakai, A.: Anomalous winter snow amplified earthquake induced disaster of the 2015 Langtang avalanche in Nepal, Nat. Hazards Earth Syst. Sci. Discuss., doi:10.5194/nhess-2016-317, in review, 2016.

Ge, L., Ng, A.H., Li, X., Liu, Y., Du, Z., and Liu, Q.: Near real-time satellite mapping of the 2015 Gorkha earthquake, Nepal, Ann. GIS, 21(3), 175–190, doi:10.1080/19475683.2015.1068221, 2015.

Goda, K., Kiyota, T., Pokhrel, R., Chiaro, G., Katagiri, T., Sharma, K., and Wilkinson, S.: The 2015 Gorkha Nepal earthquake: insights from earthquake damage survey, Front. Built. Environ. 1(8), 1–15, doi:10.3389/fbuil.2015.00008, 2015.

5   ICIMOD: Geohazards in the aftermath of the 25 April 2015 (12 Baisakh 2072) earthquake, A rapid analysis prepared for the Government of Nepal, 2015. [http://www.icimod.org/?q=18072]

ICIMOD: Villages in Langtang Valley destroyed by landslides and pressure waves during the 25 April 2015 earthquake, 2015. [http://www.icimod.org/?q=18314]

Kargel, J.S., Leonard, G.J., Shugar, D.H., Haritashya, U.K., Bevington, A., Fielding, E.J., Fujita, K., Geertsema, M., Miles,
10 E.S., Steiner, J., Anderson, E., Bajracharya, S., Bawden, G.W., Breashears, D.F., Byers, A., Collins, B., Dhital, M.R., Donnellan, A., Evans, T.L., Geai, M.L., Glasscoe, M.T., Green, D., Gurung, D.R., Heijenk, R., Hilborn, A., Hudnut, K., Huyck, C., Immerzeel, W.W., Jiang, L., Jibson, R., Kaab, A., Khanal, N.R., Kirschbaum, D., Kraaijenbrink, P.D.A., Lamsal, D., Liu, S., Lv, M., McKinney, D., Nahirnick, N.K., Nan, Z., Ojha, S., Olsenholler, J., Painter, T.H., Pleasants, M., KC, P., Yuan, Q., Raup, B.H., Regmi, D., Rounce, D.R., Sakai, A., Shangguan, D., Shea, J.M., Shrestha, A.B., Shukla, A., Stumm,
15 D., van der Kooij, M., Voss, K., Wang, X., Weihs, B., Wolfe, D., Wu, L., Yao, X., Yoder, M.R., and Young, N.: Geomorphic and geologic controls of geohazards induced by Nepal's 2015 Gorkha earthquake. Science, 351(6269), doi:10.1126/science.aac8353, 2015.

Kobayashi, T., Tobita, M., Koarai, M., Otoi, K., and Nakano, T.: Liquefaction Area Associated with the 2011 off the Pacific coast of Tohoku Earthquake, Inferred from Interferometric SAR Coherence Change, Journal of Geospatial Information
20 Authority of Japan, 122, 143–151, 2011 (in Japanese).

López-Martínez, C. and Pottier, E.: Coherence estimation in synthetic aperture radar data based on speckle noise modeling. Applied optics, 46(4), 544–558, 2007.

Ono, Y. and Sadakane, A.: Natural background of the yak transhumance in the Langtang valley, Nepal Himalaya, Geographical Reports of Tokyo Metropolitan University, 21, 95–109, 1986.

25 Lacroix, P.: Landslides triggered by the Gorkha earthquake in the Langtang valley, volumes and initiation processes, Earth, Planets and Space, 68(46), doi:10.1186/s40623-016-0423-3, 2016.

Parameswaran, R.M., Natarajan, T., Rajendran, K., Rajendran, C.P., Mallick, R., Wood, M., and Lekhak, H.C.: Seismotectonics of the April–May 2015 Nepal earthquakes: An assessment based on the aftershock patterns, surface effects and deformational characteristics, J. Asian Earth Sci., 111, 161–174, doi:10.1016/j.jseaes.2015.07.030, 2015.

30 Plank, S.: Rapid damage assessment by means of multi-temporal SAR—A comprehensive review and outlook to Sentinel-1. Remote Sensing, 6(6), 4870–4906, 2014.

Roy, B., Sathian, B., and Banerjee, I.: Nepal earthquake 2015–an overview, J. Biomed. Sci., 2(1), 1–2, doi:10.3126/jbs.v2i1.13030, 2015.

Shiraiwa, T. and Watanabe, T.: Late Quaternary glacial fluctuations in the Langtang Valley, Nepal Himalaya, reconstructed by relative dating methods, Arctic Alpine Res., 23(4), 404–416, doi:10.2307/1551682, 1991.

Shiraiwa, T.: Glacial fluctuations and cryogenic environments in the Langtang Valley, Nepal Himalaya. Contributions from the Institute of Low Temperature Science. Series A, 38, 1–98, 1994.

5   Tadono, T., Takaku, J., Tsutsui, K., Oda, F., and Nagai, H.: Status of "ALOS World 3D (AW3D)" global DSM generation, Proc. of Geoscience and Remote Sensing Symposium (IGARSS), 2015 IEEE International, 3822–3825, 2015.

Tamura, M. and El-Gharbawi, T.: Mapping damage in Shinomaki City due to the 2011 Tohoku Earthquake using InSAR coherence change, Proc. of the 58th Spring Conference of the Remote Sensing Society of Japan, 29–30, 2015 (in Japanese).

Yonezawa, C. and Takeuchi, S.: Decorrelation of SAR data by urban damages caused by the 1995 Hyogoken-nanbu
10   earthquake, Int. J. Remote Sens., 22(8), 1585–1600, 2001.

Touzi, R., Lopes, A., Bruniquel, J., and Vachon, P. W.: Coherence estimation for SAR imagery. IEEE Transactions on Geoscience and Remote Sensing, 37(1), 135–149, 1999.

Watanabe, M., Thapa, R. B., Ohsumi, T., Fujiwara, H., Yonezawa, C., Tomii, N., and Suzuki, S.: Detection of damaged urban areas using interferometric SAR coherence change with PALSAR-2. Earth, Planets and Space, 68(1), 131, 2016.

15
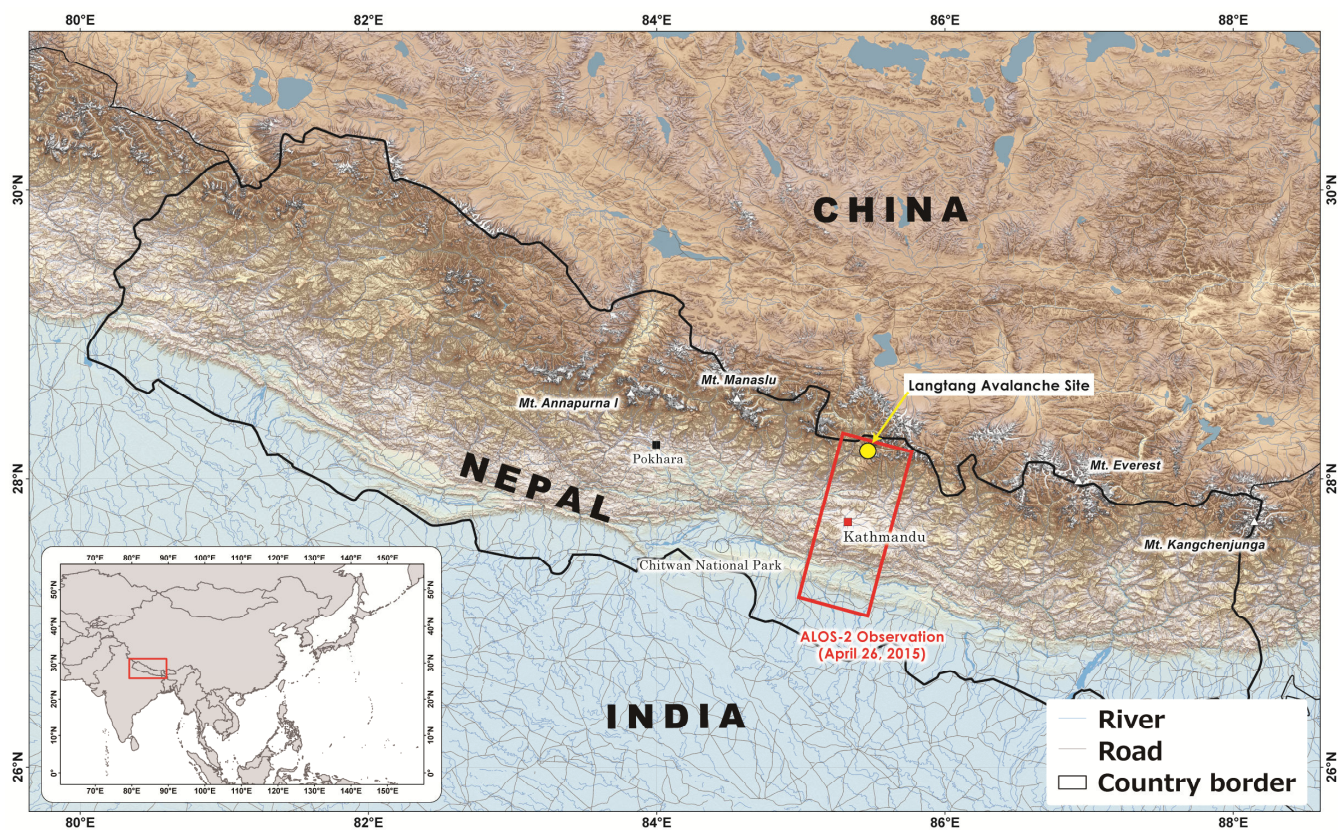
Figure 1: Location of the study site. Topography obtained from NASA/USGS SRTM3v4, glacier outlines obtained from ICIMOD Mountain Geoportal, rivers and roads obtained from DIVA-GIS, and country borders obtained from ThematicMapping.org are illustrated.

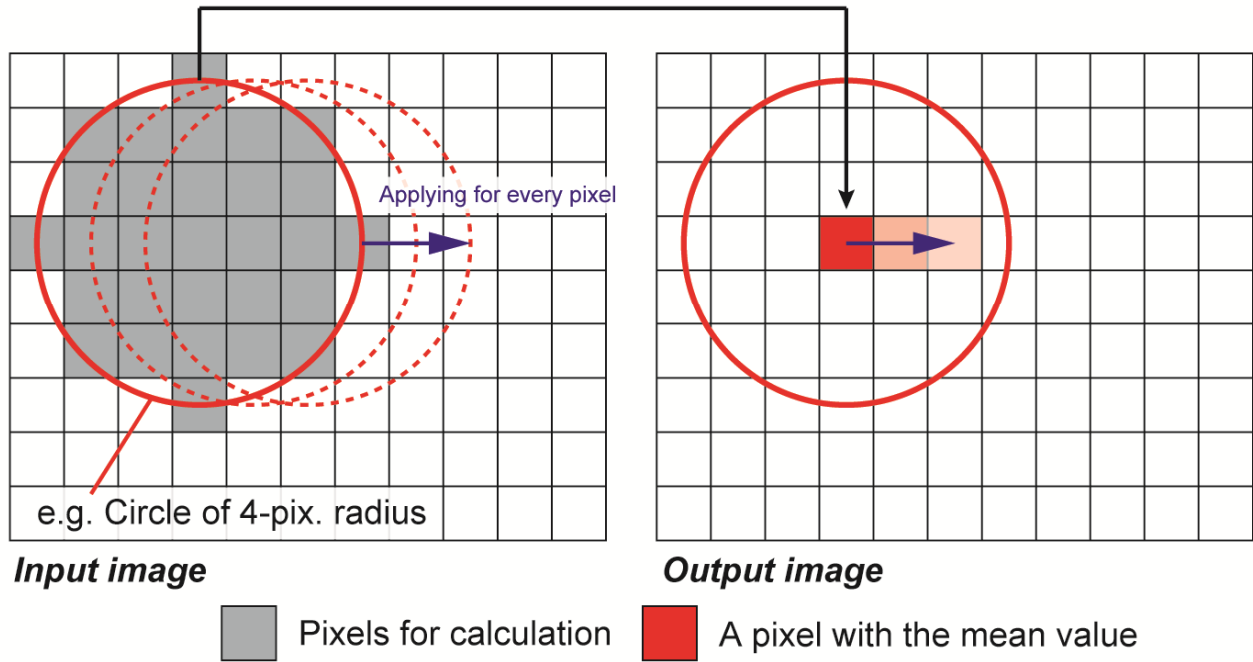The mean value of pixels inside a circle is put at the center pixel.

Applying for every pixel

e.g. Circle of 4-pix. radius

Input image

Output image

Pixels for calculation   A pixel with the mean value

Figure 2: Concept of focal statistics filter to reduce noises.
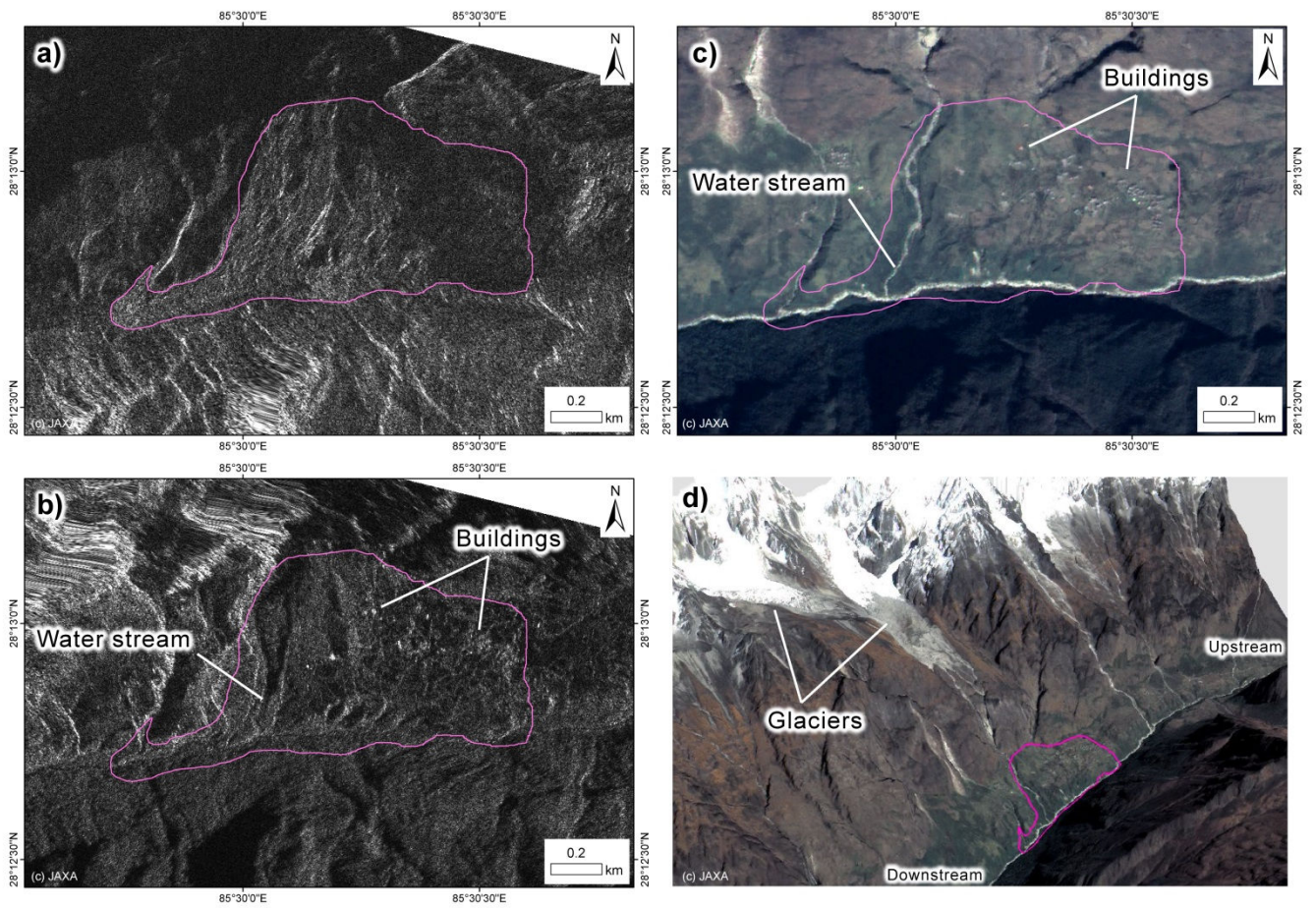
14

Figure 3: Identified collapsed sediment by ALOS/ALOS-2 images. Difference between PALSAR-2 images of (a) post-quake (April 26, 2015) and (b) pre-quake (December 28, 2014) denotes that the buildings and water stream identifiable by (c) a pre-quake ALOS pan-sharpened image (October 12, 2008) has been covered by the sediments. (d) A three-dimensional view of the ALOS pan-sharpened image overlaid on ALOS World 3D digital surface model.
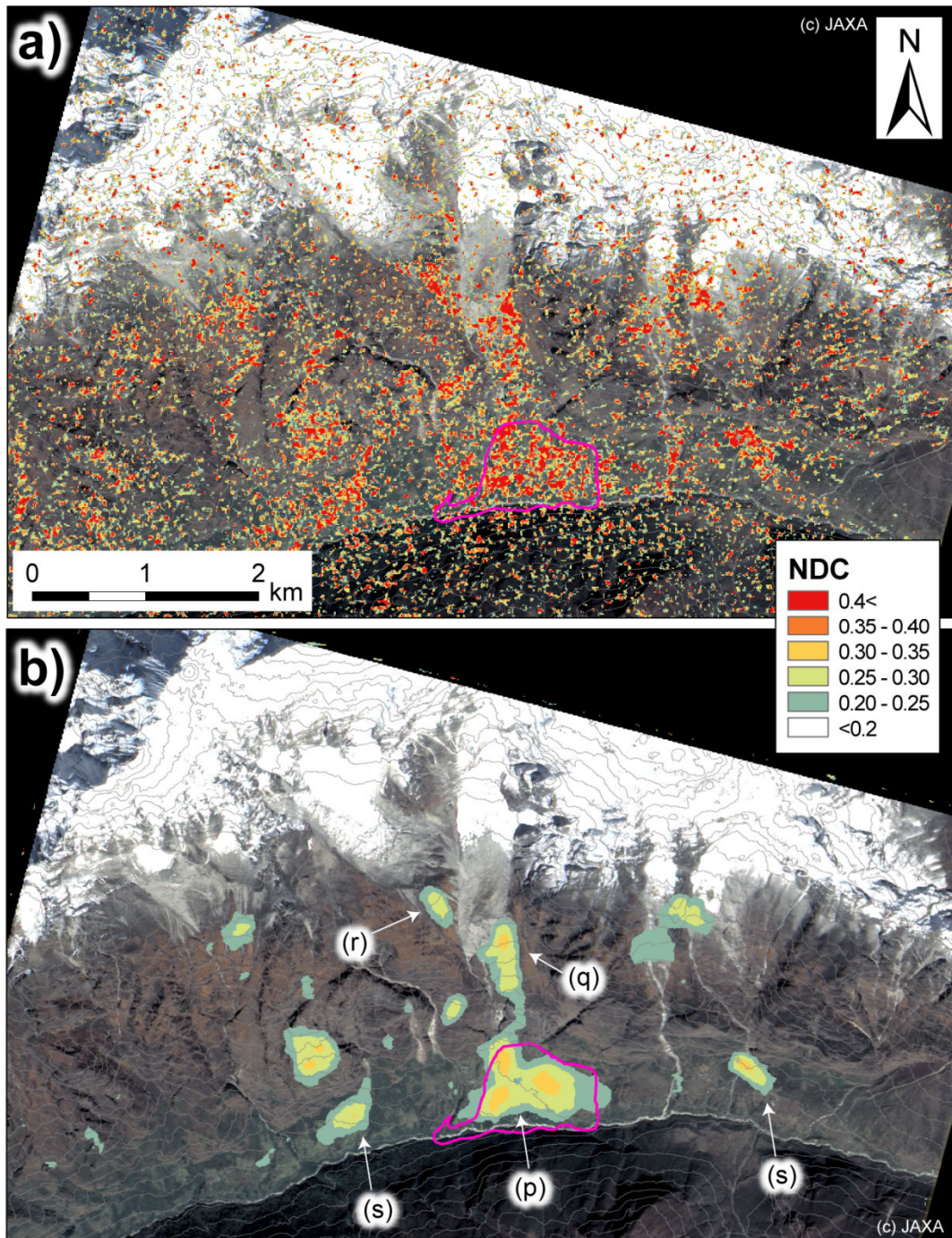
Figure 4: Normalized coherence decrease around the collapsed area in Langtang Valley. (a) Original output image is processed into two images of focal statistics with (b) 15-m circles for calculating the mean values. High-value parts are denoted on (p) the collapse area, (q) a glacier moraine, and (r) that of a tributary glacier, as well as (s) two places in the valley bottom. The background is an ALOS pan-sharpened image observed on October 12, 2008.
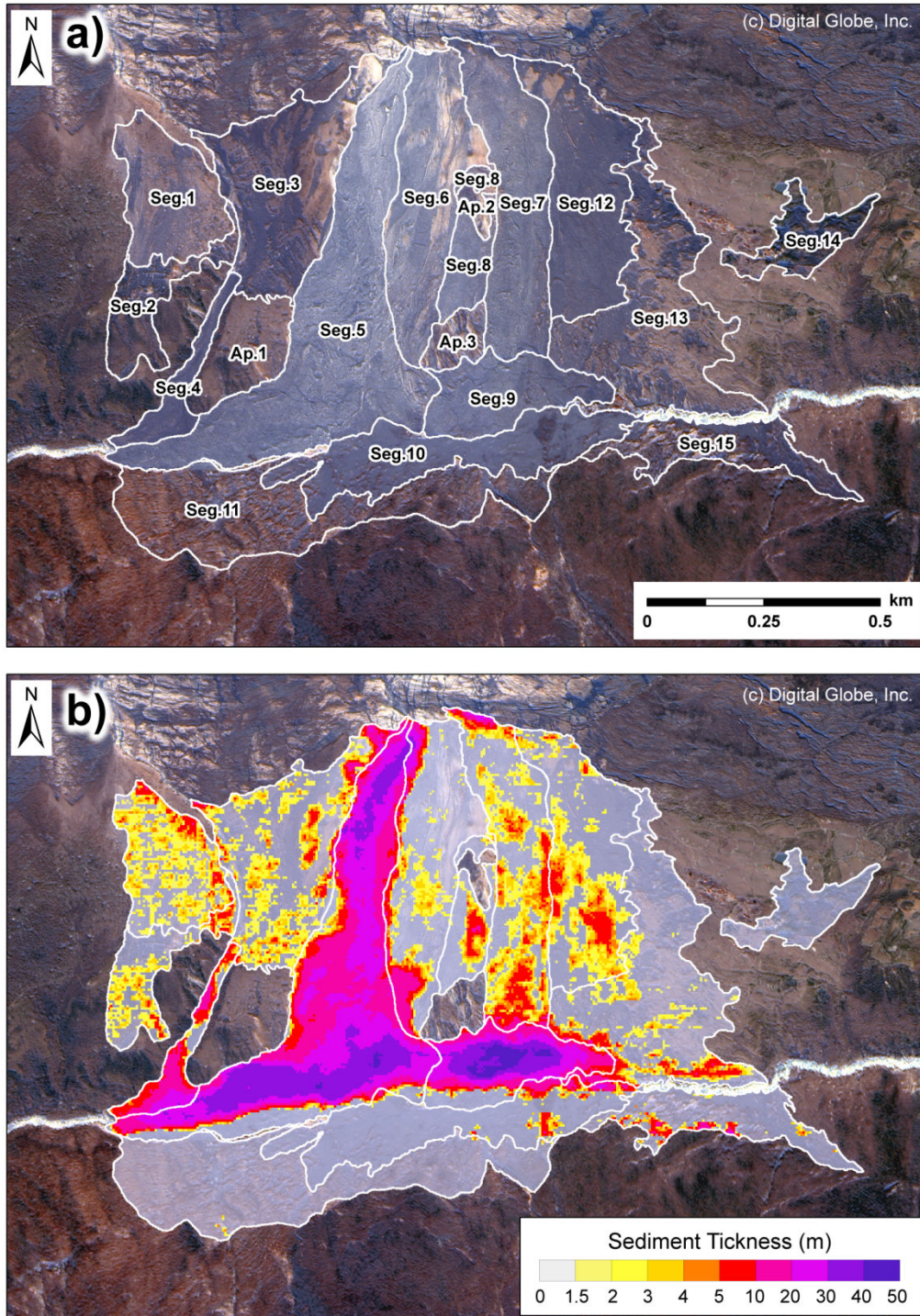
16

Figure 5: (a) Sediments classified into 15 segments (Seg. 1 to 15) and 3 little-covered segments (Ap. 1 to 3), which were interpreted from a WorldView-3 (WV-3) image acquired on May 8, 2015. (b) Estimation of the sediment volume from the altitude difference between pre-event ALOS World 3D DSM and post-event WV-3 DSM.
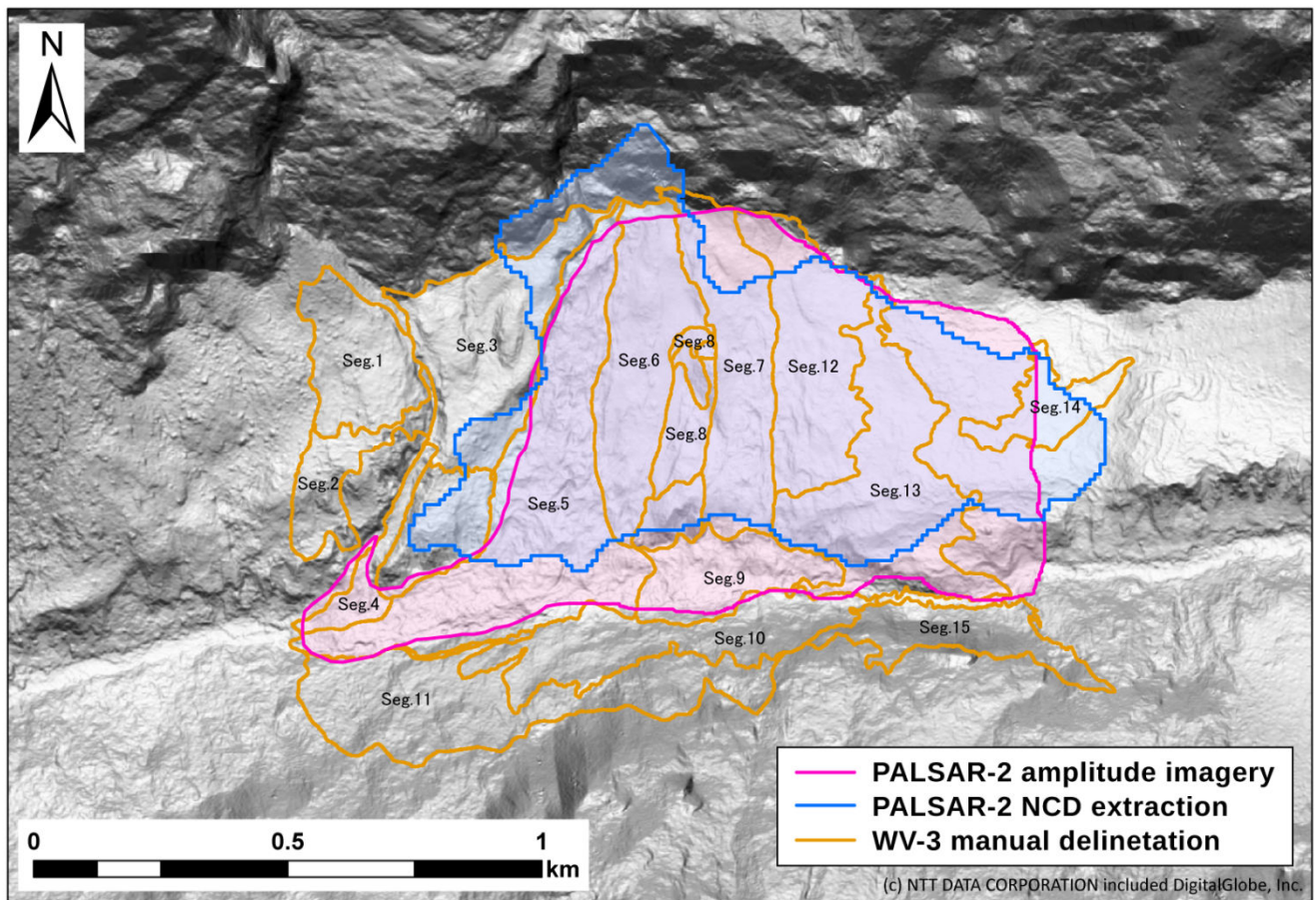
Figure 6: Sediment outlines delineated from PALSAR-2 data (purple for amplitude imagery and blue for coherence calculation) and WorldView-3 (WV-3) imagery (orange). The background is hill-shade imagery generated from the WV-3 DSM.
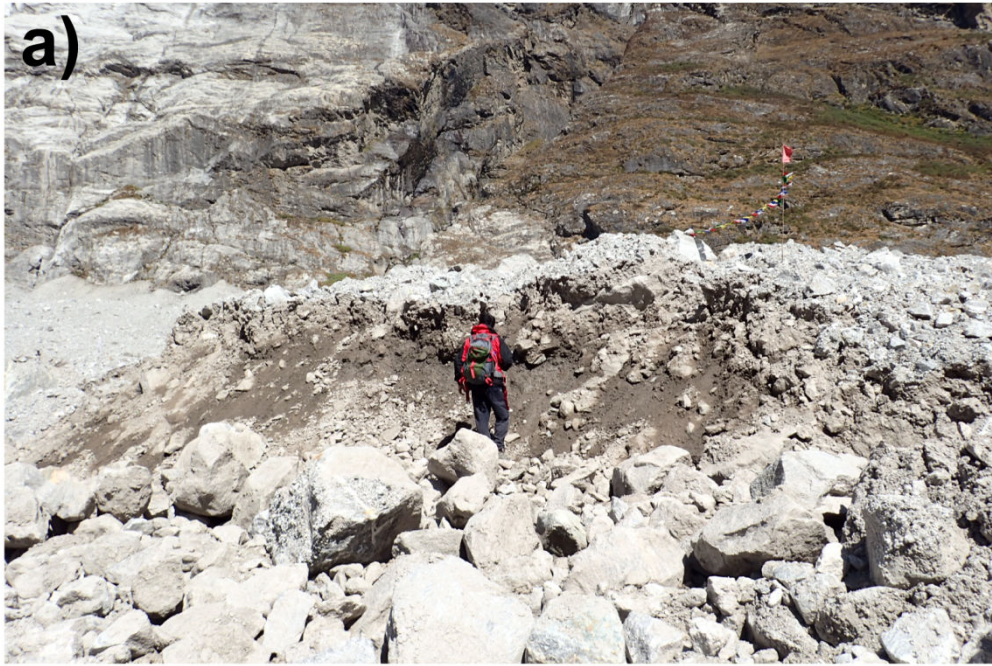
Figure 7. (a) A picture on the avalanche-induced sediment surface taken in an in-situ survey carried out for/by Fujita et al. (2016). (b) A closed-up picture showing exposed and melting ice. [Date: Oct. 21, 2015]

19

Table 1: Area, thickness, volume, and identified surface features of 15 classified segments of the collapses sediments.

Segment	Area (x10³ m³)	Thickness (m) Max	Thickness (m) Mean				Volume (x10³ m³) (	Min.	–	Max.	)	Darkness	Flow or Scatter	Surface character
1	54.2	12.0	2.3	±	1.6	124.5	(	57.5	–	204.2	)	Dark	Scatter	
2	32.1	9.8	1.7	±	1.8	55.3	(	25.7	–	96.9	)	Dark	Scatter	
3	98.2	25.2	2.2	±	3.0	216.3	(	122.3	–	344.7	)	Dark	Scatter	
4	19.7	30.2	11.0	±	7.6	218.0	(	190.8	–	246.1	)	Dark	Flow	
5	178.5	42.1	20.3	±	10.6	3612.6	(	3365.5	–	3863.4	)	Light	Flow	Boulders
6	85.8	34.6	3.0	±	5.6	255.5	(	195.0	–	347.6	)	Light	Flow	Streak
7	87.1	29.7	2.9	±	3.2	250.6	(	153.3	–	369.2	)	Mediam	Flow	Boulders
8	22.1	11.1	1.7	±	2.4	37.3	(	22.0	–	59.5	)	Mediam		
9	46.9	46.7	22.0	±	13.6	1036.5	(	974.5	–	1099.7	)	Mediam	Flow	Muddy
10	75.3	24.3	1.2	±	3.5	91.5	(	72.8	–	114.3	)	Mediam		Muddy
11	114.8	4.9	0.0	±	0.2	2.1	(	0.8	–	4.3	)	Mediam	Scatter	
12	87.3	9.6	1.7	±	1.9	150.7	(	75.3	–	258.3	)	Dark		
13	116.6	17.1	1.2	±	2.4	141.6	(	81.9	–	250.8	)	Dark	Scatter	
14	27.1	1.1	0.0	±	0.1	0.2	(	0.0	–	6.2	)	Dark	Scatter	
15	42.4	25.4	0.9	±	2.6	36.4	(	26.1	–	49.6	)	Dark	Scatter	
Total	1088.1	46.7				6229.1	(	5363.3	–	7314.8	)			